

See discussions, stats, and author profiles for this publication at: <https://www.researchgate.net/publication/228978074>

# Growth and Desorption Kinetics of Ultrathin Zn Layers on Pd (111)

ARTICLE in THE JOURNAL OF PHYSICAL CHEMISTRY C · JUNE 2009

Impact Factor: 4.77 · DOI: 10.1021/jp9017376

CITATIONS

27

READS

29

10 AUTHORS, INCLUDING:



**Markus Kratzer**

Montanuniversität Leoben

29 PUBLICATIONS 181 CITATIONS

SEE PROFILE



**Anton Tamtögl**

University of Cambridge

14 PUBLICATIONS 125 CITATIONS

SEE PROFILE



**Imre Bakó**

Hungarian Academy of Sciences

91 PUBLICATIONS 1,565 CITATIONS

SEE PROFILE

# Growth and Desorption Kinetics of Ultrathin Zn Layers on Pd(111)

G. Weirum,<sup>†,‡</sup> M. Kratzer,<sup>†</sup> H. P. Koch,<sup>†,§</sup> A. Tamtögl,<sup>†</sup> J. Killmann,<sup>†</sup> I. Bako,<sup>§</sup> A. Winkler,<sup>†</sup> S. Surnev,<sup>‡</sup> F. P. Netzer,<sup>‡</sup> and R. Schennach<sup>\*,†</sup>

*Institute of Solid State Physics, Graz University of Technology, A-8010 Graz, Austria, Institute of Physics, Karl-Franzens University Graz, A-8010 Graz, Austria, and Chemical Research Centre, Hungarian Academy of Science, H-1025 Budapest, Hungary*

*Received: February 25, 2009; Revised Manuscript Received: April 20, 2009*

A scanning tunneling microscopy (STM) study, combined with density functional theory (DFT) calculations and thermal desorption spectroscopy (TDS) data, on the growth and structure of Zn on a Pd(111) surface is presented. The STM results demonstrate that PdZn(111) surface alloy bilayer islands with a  $p(2 \times 1)$  structure already form during the room temperature deposition of submonolayer amounts of Zn on Pd(111). DFT calculations predict that the PdZn bilayers are energetically more stable than single PdZn layers and establish their structural parameters. The TDS data show that Zn desorbs below 600 K in a multiple-peak desorption structure with fractional order desorption kinetics of the individual components, which is due to multilayer Zn desorption. The experimentally derived adsorption energies of the low temperature desorption peaks are reproduced in the DFT calculations. At temperatures above 750 K, Zn desorbs from the PdZn alloy, and the desorption kinetics is a mixture of a first-order and a diffusion-limited desorption process.

## 1. Introduction

Pd/ZnO catalysts have recently received growing attention for hydrogen production in the methanol steam reforming (MSR) process and have been considered as an alternative of the traditionally used low-cost Cu/ZnO catalysts. The Pd/ZnO system offers several advantages, such as higher thermal stability and an enhanced activity and selectivity for MSR, as compared to Cu/ZnO catalysts.<sup>1,2</sup> It has been proposed that a PdZn alloy, forming during the thermal reduction of ZnO, is one of the active components responsible for this high catalytic performance of the Pd/ZnO catalysts.<sup>3,4</sup> Pd and Zn are miscible, and several stable PdZn bulk alloys are known to form with different compositions and structures,<sup>5</sup> among them a phase with an atomic ratio of Pd to Zn close to 1:1 and with the CuAu-L1<sub>0</sub> structure, which is thermally the most stable one.<sup>6</sup> The structure and stability of various surfaces of the PdZn (1:1) alloy, the segregation propensity of Pd–Zn films, and the chemical reactivity of PdZn surfaces have been recently investigated with DFT calculations by Rösch et al.<sup>7–9</sup> The calculated surface energies<sup>7</sup> have indicated that the (111) surface is thermodynamically the most stable one, exposing a stoichiometric layer of alternating close-packed Pd and Zn rows. Bayer et al.<sup>10</sup> have first studied experimentally the growth and the structure of PdZn surface alloys, which form upon deposition of Zn on a Pd(111) surface, followed by a thermal annealing step. They have attributed the observed  $(2 \times 2)$  LEED pattern to the formation of an ordered  $p(2 \times 1)$  PdZn(1:1) surface alloy structure, which has been supported by X-ray photoelectron spectroscopy (XPS) analysis. The electronic structure of this PdZn surface alloy is strongly modified with respect to that of metallic Pd and exhibits a significant reduction of the density of Pd 4d states near the Fermi level, in line with previous observations.<sup>11,12</sup> In a

subsequent study, Gabasch et al.,<sup>13</sup> on the basis of thermal desorption spectroscopy (TDS) data, have interpreted this  $(2 \times 2)$  LEED pattern instead as due to a  $p(2 \times 2)$ -3Zn surface adlayer. This conclusion has been questioned by Jerro et al.,<sup>14</sup> whose LEED, TDS, and high-resolution electron energy loss spectroscopy (HREELS) results have favored again the formation of a  $(2 \times 1)$  surface PdZn alloy upon heating of Zn layers on Pd(111). The latter seems to be the consensus result at present, as also recently confirmed by the low energy ion scattering (LEIS) data of Stadlmayr et al.<sup>15</sup>

Here we report on the first scanning tunneling microscopy (STM) study of the growth and the structure of Zn on the Pd(111) surface, which is combined with thermal desorption spectroscopy (TDS) data and density functional theory (DFT) calculations. The STM results demonstrate that PdZn(111) surface alloy bilayer islands with a  $p(2 \times 1)$  structure already form during the room temperature deposition of submonolayer amounts of Zn on Pd(111). The PdZn bilayer is only stable upon annealing to 450 K and decomposes at higher temperatures because of the dissolution of Zn in the Pd bulk. The DFT calculations establish the structure and energetics parameters of PdZn layers on Pd(111) and show that the PdZn bilayers exhibit a lower surface energy with respect to the single PdZn layer. The Zn TD spectra exhibit a low temperature desorption feature between 400 and 600 K, and a high temperature peak above 750 K. The adsorption energies of the different TDS peaks have been analyzed and have been reproduced in the DFT calculations.

## 2. Experimental and Computational Details

STM experiments have been carried out in a UHV chamber equipped with crystal cleaning, metal evaporation, LEED, and STM facilities. The STM (Omicrometer, micro-STM) was operated in the constant current mode at room temperature. The STM tips were fabricated from 0.3 mm W wire by electrochemical etching and cleaned in situ by electron bombardment heating. Clean Pd(111) crystal surfaces were prepared by cycles

\* Corresponding author. E-mail: robert.schennach@tugraz.at, phone +43 316 873 8462, fax +43 316 873 8466.

<sup>†</sup> Graz University of Technology.

<sup>‡</sup> Karl-Franzens University Graz.

<sup>§</sup> Hungarian Academy of Science.

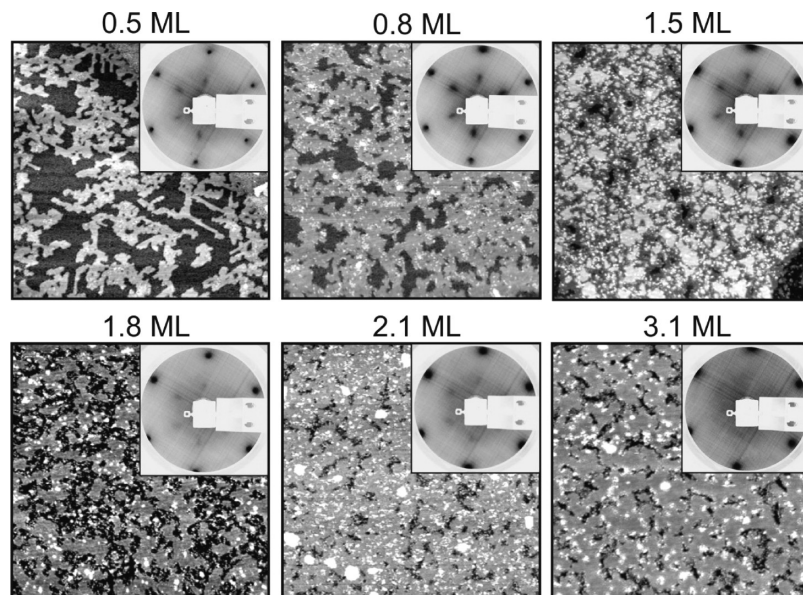


**Figure 1.** Large-scale STM images ( $1000 \text{ \AA} \times 1000 \text{ \AA}$ ) of Zn films grown at 300 K on Pd(111): 0.5 ML ( $U = +1.0 \text{ V}$ ;  $I = 0.4 \text{ nA}$ ); 0.8 ML ( $U = -1.0 \text{ V}$ ;  $I = 0.4 \text{ nA}$ ); 1.5 ML ( $U = -1.0 \text{ V}$ ;  $I = 0.4 \text{ nA}$ ); 1.8 ML ( $U = -1.0 \text{ V}$ ;  $I = 0.4 \text{ nA}$ ); 2.1 ML ( $U = -1.0 \text{ V}$ ;  $I = 0.4 \text{ nA}$ ); 3.1 ML ( $U = -1.0 \text{ V}$ ;  $I = 0.4 \text{ nA}$ ). The corresponding LEED patterns are shown in the insets: 0.5 ML ( $E = 63.7 \text{ eV}$ ); 0.8 ML ( $E = 61.6 \text{ eV}$ ); 1.5 ML ( $E = 56.3 \text{ eV}$ ); 1.8 ML ( $E = 67.0 \text{ eV}$ ); 2.1 ML ( $E = 56 \text{ eV}$ ); 3.1 ML ( $E = 55.7 \text{ eV}$ ).

of  $\text{Ar}^+$ -ion bombardment (1.5 kV) and UHV annealing to 1000 K. To remove residual carbon, the crystal was annealed at temperatures between 400 and 900 K in an oxygen pressure of  $2 \times 10^{-7}$  mbar, followed by a final flash to 1100 K in UHV.

The thermal desorption (TD) kinetics experiments were carried out in a second ultrahigh vacuum (UHV) chamber with a base pressure of  $2 \times 10^{-10}$  mbar. The chamber was equipped with an Auger electron spectrometer (AES), a low energy electron diffraction (LEED) optics, and an  $\text{Ar}^+$ -ion sputtering gun. A quadrupole mass spectrometer (QMS) was installed in the main chamber for residual gas analysis and monitoring the preparation steps. In a differentially pumped detector chamber (base pressure  $7 \times 10^{-11}$  mbar) a second quadrupole mass spectrometer was mounted in a line-of-sight (LOS) configuration for thermal desorption spectroscopy (TDS). The Pd sample was a (111) oriented single crystal disk with a diameter of 10 mm and a thickness of 1.5 mm. The sample was mounted on a sample holder by tantalum wires ( $\phi 0.25 \text{ mm}$ ) which could be heated resistively. The sample holder was attached to a manipulator which allowed a positioning in front of all analytical devices. The whole assembly could be cooled by liquid nitrogen. The minimum attainable sample temperature was 105 K, and the maximum temperature was 1180 K. Sample cleaning was performed by several cycles of  $\text{Ar}^+$ -ion bombardment at an ion energy of 0.6 keV slightly below room temperature to avoid penetration of the residual zinc into the sample. Subsequently the sample was annealed by flashing it up to 1180 K with a heating rate of 2 K/s. The same heating rate was typically used for thermal desorption spectroscopy. The purity and the surface geometry were checked by Auger electron spectroscopy (AES) and low energy electron diffraction (LEED), respectively. Small carbon contaminations on palladium are hardly detectable because of the overlap of the carbon Auger peak at 272 eV with the palladium peak at 278 eV. Therefore, additional CO thermal desorption experiments were carried out which are very sensitive to contamination on the surface.<sup>13,14,16,17</sup>

For Zn deposition, home-built Knudsen cells were used in both UHV systems by resistively heating molybdenum or BN (STM system) crucibles filled with pieces of a Zn wire (99.98%,

Goodfellow). The rate of deposition was tuned by varying the temperature of the cell and monitored by a quartz microbalance. Given the difficulties in applying the quartz microbalance for a reliable thickness control of the Zn films, described in our previous work,<sup>16</sup> the Zn deposition rate has been cross-calibrated by monitoring the Zn QMS signal (mass 64) in the isotropic gas phase or by measuring in STM the area of two-dimensional Zn islands at coverages above 2 ML, where metallic Zn grows at room temperature in a layer-by-layer mode (see, e.g., Figure 1).

Density functional theory (DFT) calculations were carried out to get a more complete picture of the structure and the energetics of the Zn–Pd(111) surfaces. For this purpose the Vienna ab initio simulation package (VASP)<sup>18–22</sup> was used utilizing the PW91 generalized gradient approximation (GGA).<sup>23</sup> The Pd(111) substrate was modeled by a four-layer thick slab with a vacuum spacing larger than 20 Å. The PdZn surface alloy was simulated by additional layers forming a  $(2 \times 1)$ -PdZn structure. In order to check if four Pd layers are enough, calculations with only three layers of Pd instead of four were made, which yielded the same results. For most of the calculations one layer consisted of four atoms (enabling a  $(2 \times 2)$  structure) which allowed one to test the influence of the coverage down to 1/4 ML. For the slab model calculations a  $(7 \times 7 \times 1)$  Monkhorst Pack<sup>24</sup> grid was applied in combination with the Methfessel–Paxton smearing<sup>25</sup> with a default smearing width of 0.2 eV. The energy cutoff was set to 400 eV for all presented results. Furthermore, the atomic coordinates of the adsorbates were optimized until the force acting on each atom became less than 0.01 eV/Å. For the calculation of the density of states a  $(15 \times 15 \times 1)$  k-point grid was used.

For comparison of theoretical and experimental results, STM simulations were done using the multiple scattering method<sup>26</sup> incorporated into the Tersoff–Haman approach.<sup>27,28</sup> For these calculations we used BSKAN 3.6<sup>29,30</sup> which is an optimized and parallel code to simulate STM topography and spectroscopy from first principles. For these calculations the PBE functional<sup>31,32</sup> was used. The difference between the two functionals used was not significant. The adsorption energies were calculated as

$$\Delta E_{\text{ads}} = E_{\text{total}} - E_{\text{adsorbate}} + E_{\text{substrate}} \quad (1)$$

where  $\Delta E_{\text{ads}}$  is the adsorption energy,  $E_{\text{adsorbate}}$  is the energy of the unbound adsorbate,  $E_{\text{substrate}}$  is the energy of the substrate without the adsorbate, and  $E_{\text{total}}$  is the total energy of the whole system (adsorbate and substrate). The surface energy was calculated according to the formula given by Röscher et al.,<sup>7</sup> which can be written in the following form:

$$\gamma = (E_{\text{S}}^{\text{N}} - \sum_{i=1}^{\text{N}} E_{\text{L}}^i) / 2A \quad (2)$$

Here  $\gamma$  is the surface energy,  $E_{\text{S}}^{\text{N}}$  is the energy of the total slab,  $E_{\text{L}}^i$  is the energy of the  $i$ th layer, and  $A$  is the surface area of the unit cell. Using this approach we get a surface energy for Pd(111) of  $1.40 \text{ J m}^{-2}$ , which compares very good to the value of  $1.38 \text{ J m}^{-2}$  reported by Röscher et al.<sup>7</sup> The energy of a Zn hole in the surface was calculated in the following way:

$$E_{\text{hole}} = E_{\text{total(hole)}} - E_{\text{layer(hole)}} - E_{\text{substrate}} \quad (3)$$

Here  $E_{\text{hole}}$  is the energy of the hole in the surface layer,  $E_{\text{total(hole)}}$  is the calculated total energy of the slab with the hole in the surface with the same geometry as in the system,  $E_{\text{layer(hole)}}$  is the energy of the surface layer with the hole, and  $E_{\text{substrate}}$  is the energy of the substrate below the layer with the hole.

### 3. Results and Discussion

#### 3.1. Growth and Structure of Zn–Pd(111) Surfaces.

Figure 1 shows a set of large-scale ( $1000 \text{ \AA} \times 1000 \text{ \AA}$ ) STM images, illustrating the growth morphology of Zn overlayers deposited on the Pd(111) surface at room temperature (300 K). At submonolayer Zn coverages,  $\Theta_{\text{Zn}}$ , two-dimensional (2D) islands form, which exhibit dendritic shapes, indicative of a diffusion-limited growth process. LEED images (see corresponding insets in Figure 1) show at 0.5 ML a weak  $(2 \times 2)$  pattern, which becomes more intense as  $\Theta_{\text{Zn}}$  increases to 0.8 ML. At this Zn coverage, the growth of a second layer sets in, before the completion of the first layer. The second layer grows in a more compact fashion than the first one and is almost fully closed at  $\Theta_{\text{Zn}} = 2.1 \text{ ML}$ . The  $(2 \times 2)$  LEED pattern becomes weaker again and transforms gradually to a  $(1 \times 1)$  pattern. Eventually, after 3.1 ML, the third layer is more or less completed, i.e., the uptake of Zn on Pd(111) at 300 K follows a quasi-layer-by-layer growth mode above 2 ML. This is also evident from Figure 2, where the coverage of the first three layers, as measured from their corresponding areas of the STM images in Figure 1, has been plotted against the total deposited Zn coverage. Here, the ideal layer-by-layer growth behavior (straight lines) has been also displayed for comparison. The uptake curves of the first two Zn layers, where the  $(2 \times 2)$  structure is visible in the LEED images, clearly deviate from the layer-by-layer mode, whereas the growth curve of the third layer resembles more closely a straight line.

The STM images in Figure 3 reveal details of the surface structure of the Zn overlayers. At submonolayer Zn coverages, the islands exhibit a stripe structure, with the stripes running along three equivalent  $\langle 110 \rangle$  substrate directions and separated from each other by  $\sim 4.8 \text{ \AA}$ . This distance corresponds to twice the separation between neighboring  $\langle 110 \rangle$  rows on the Pd(111) surface (i.e.,  $\sqrt{3} \times a_{\text{Pd(111)}}$ , with  $a_{\text{Pd(111)}} = 2.75 \text{ \AA}$ ). Atomically resolved STM images (see the inset of the image at 0.8 ML

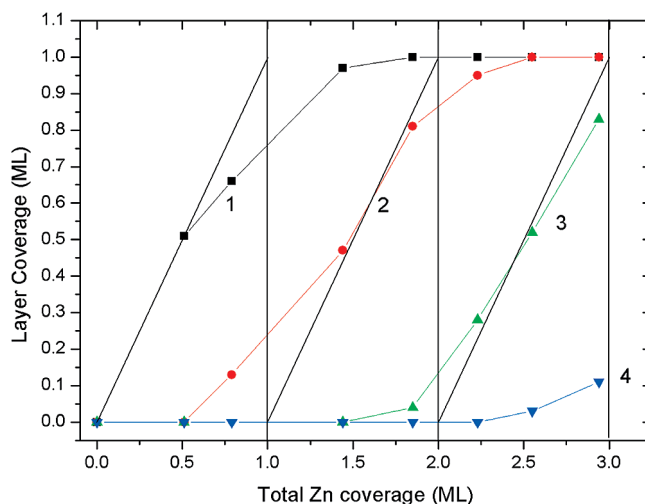


**Figure 2.** Plot of the layer coverage versus the total Zn coverage. The numbers indicate the corresponding layers. The straight lines reproduce an ideal layer-by-layer uptake.

and Figure 6a) show that the spacing along the stripes is equal to  $a_{\text{Pd(111)}}$ , which means that the submonolayer Zn islands exhibit a  $p(2 \times 1)$  structure. At 1.5 ML the  $p(2 \times 1)$  periodicity is visible in the first layer, as well as on some of the islands of the second layer. Above 2 ML no  $p(2 \times 1)$  structure can be discerned anymore: the islands are atomically flat and their surface exhibits a very low corrugation ( $<5 \text{ pm}$ ) in the STM images, implying a closely packed Zn overlayer. The presence of  $p(2 \times 1)$  domains in three equivalent crystallographic substrate directions in the Zn coverage range up to 1.5 ML generates the observed  $(2 \times 2)$  LEED pattern. Our STM results thus unambiguously support the  $p(2 \times 1)$ -PdZn alloy model, proposed by Bayer et al.<sup>10</sup> The  $p(2 \times 1)$  structure forms on the Pd(111) surface already during the Zn deposition at 300 K, which is the onset temperature of the PdZn alloy formation, according to the XPS results of Bayer et al.<sup>10</sup> The dendritic shape of the  $p(2 \times 1)$  islands can be understood as a result of hindered diffusion of Zn adatoms along the perimeter of the islands because of a preferential exchange process with the Pd surface atoms. The latter process is kinetically constrained at room temperature mainly at the Pd–Zn interface, as evidenced by the STM and LEED data of Figure 1, which show that beyond 2 ML, metallic Zn growth commences in a layer-by-layer fashion on top of the PdZn surface alloy, causing the disappearance of the  $(2 \times 2)$  pattern. Recently, a ZnAu surface alloy formation has been reported by Freyland et al. for electrodeposited Zn on a Au(111) surface.<sup>33,34</sup> Their in situ electrochemical STM observations reveal labyrinth-like two-dimensional structures, which indicates that the ZnAu alloying occurs via a spinodal decomposition process.<sup>34</sup>

The coverage and the height of the  $(2 \times 1)$ -PdZn surface alloy islands forming at submonolayer Zn coverages on the Pd(111) surface deserve to be addressed in more detail. Figure 4, parts a and b, shows large-scale and high-resolution STM images, respectively, of a 0.5 ML Zn layer deposited at 300 K on the Pd(111) surface. The relative surface area of the dendritic islands measures  $0.55 \pm 0.05\%$ , and this suggests that in order to conform with the 1:1 PdZn alloy stoichiometry only about 1/2 of the deposited Zn atoms should be present on the island's surface; the rest should be located in the layer beneath, i.e., incorporated in the Pd(111) surface. The latter Zn atoms must have exchanged place with Pd surface atoms, which in turn become bound to the Zn atoms in the islands, thus resulting in



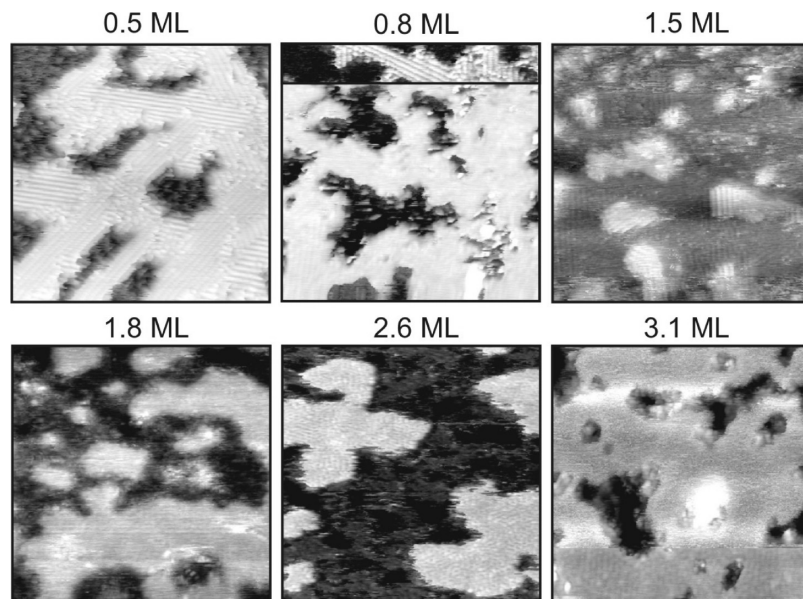


**Figure 3.** High-resolution STM images ( $200 \text{ \AA} \times 200 \text{ \AA}$ ) of Zn films grown at 300 K on Pd(111): 0.5 ML ( $U = +0.14 \text{ V}$ ;  $I = 2.0 \text{ nA}$ ); 0.8 ML ( $U = -0.3 \text{ V}$ ;  $I = 0.4 \text{ nA}$ ); inset ( $200 \text{ \AA} \times 70 \text{ \AA}$ ;  $U = -0.03 \text{ V}$ ;  $I = 7.5 \text{ nA}$ ); 1.5 ML ( $U = -0.03 \text{ V}$ ;  $I = 15 \text{ nA}$ ); 1.8 ML ( $U = -0.03 \text{ V}$ ;  $I = 14 \text{ nA}$ ); 2.6 ML ( $U = -0.3 \text{ V}$ ;  $I = 5.0 \text{ nA}$ ); 3.1 ML ( $U = -0.3 \text{ V}$ ;  $I = 1.0 \text{ nA}$ ).

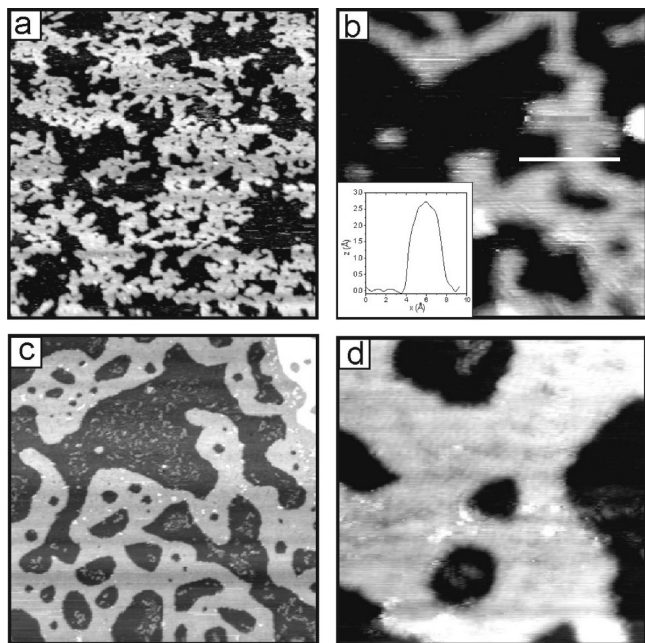


**Figure 4.** STM images of 0.5 ML Zn on Pd(111). As-deposited at 300 K: (a) ( $1000 \text{ \AA} \times 1000 \text{ \AA}$ ,  $U = +1.0 \text{ V}$ ;  $I = 0.4 \text{ nA}$ ), (b) ( $200 \text{ \AA} \times 200 \text{ \AA}$ ,  $U = +3 \text{ mV}$ ;  $I = 20 \text{ nA}$ ). Inset: Line profile taken along the white line indicated on the image b. After annealing to 450 K: (c) ( $1000 \text{ \AA} \times 1000 \text{ \AA}$ ,  $U = +1.0 \text{ V}$ ;  $I = 0.4 \text{ nA}$ ), (d) ( $200 \text{ \AA} \times 200 \text{ \AA}$ ,  $U = +0.1 \text{ V}$ ;  $I = 2.0 \text{ nA}$ ).

the formation of a PdZn bilayer. Such a model is also consistent with the apparent height of  $2.5 \pm 0.2 \text{ \AA}$  of the alloy islands, measured with respect to the bare Pd(111) areas (see line profile in the inset of Figure 4b). This value is close to the monatomic height of Pd layers ( $2.3 \text{ \AA}$ ). The PdZn bilayer islands are stable on annealing up to 450 K, above this temperature they decompose. This is exemplified in the STM images of Figure 4c, d, which have been taken after heating the 0.5 ML PdZn surface to 500 K. The island shapes change upon heating from dendritic to more compact, but their surface area remains unchanged. The high-resolution image (Figure 4d) shows that the original  $(2 \times 1)$  structure is now replaced by a close-packed

one, with a corrugation of below 50 pm, which is also consistent with the change of the LEED pattern from  $(2 \times 2)$  to  $(1 \times 1)$ . We propose that the close-packed islands consist exclusively of Pd atoms, which have been replaced by Zn atoms during their diffusion into deeper (subsurface) Pd layers and segregated on top of the Pd(111) surface. The conservation of the surface area of the islands upon this structural change simply reflects the fact that 0.5 ML Zn atoms in the  $(2 \times 1)$ -PdZn bilayer substitute the same amount of Pd atoms in a  $(1 \times 1)$ -Pd adlayer.

We have calculated the equilibrium structure of one and two monolayers of stoichiometric PdZn on Pd(111), and the corresponding DFT models (side views) are displayed in Figure 5. The calculated vertical atomic displacements, lateral separation between Pd–Pd (Zn–Zn) rows, and surface energies are collected in Table 1. Structural and energy parameters for the bulk PdZn(111) alloy, derived in our calculations, are also listed in the table and agree well with values of previous DFT calculations.<sup>7</sup> For the 1 ML PdZn layer, the Pd atoms move slightly outward with respect to their vertical position on the Pd(111) surface, whereas the Zn atoms relax inward (into the bulk). For the 2 ML PdZn slab, the situation on the surface layer is reverted, with the Zn atoms sticking out, similar to the PdZn bulk structure. The calculated surface energy of 1 ML PdZn films is virtually identical to that of the bare Pd(111) surface ( $1.40 \text{ J m}^{-2}$ ), but lowers down to  $1.22 \text{ J m}^{-2}$  for two PdZn layers, signaling their higher energetic stability on the Pd(111) surface. The structure found in the calculations for 2 ML has been recently confirmed by low energy ion spectroscopy (LEIS).<sup>15</sup> Also our STM results favor a bilayer PdZn structure on Pd(111). In Figure 6 we compare atomically resolved experimental (a) and simulated (b) STM images of 2 ML PdZn surface alloy layers. The simulated constant current STM image, which has been calculated at a bias voltage of  $+0.5 \text{ V}$ , shows rows of protrusions which correspond to the positions of the Pd atoms on the 2 ML PdZn surface, i.e., the contrast observed in the STM image is opposite to the surface topography (Pd surface atoms are lower than the Zn atoms). The image contrast turned out to be independent of the tunnelling conditions used in the simulations (polarity or magnitude of the bias voltage, tunnelling current), in agreement with the experiment. The

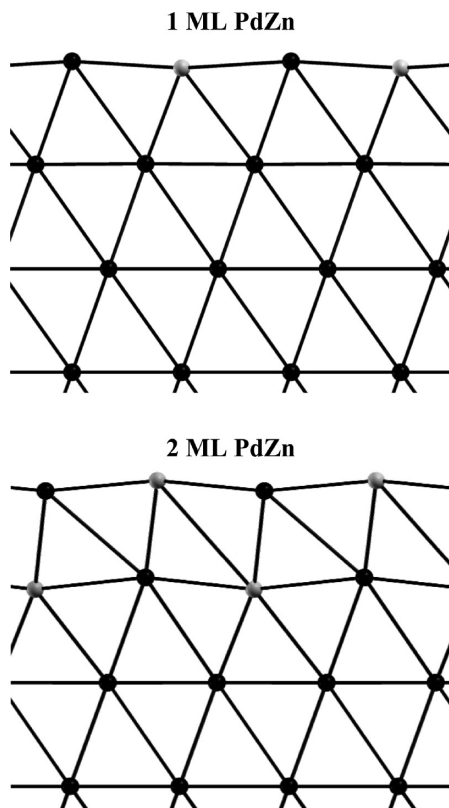


**Figure 5.** Calculated structure of PdZn surface alloys with 1 ML (top) and 2 ML (bottom). The light gray balls are the Zn atoms, and the black balls are the Pd atoms.

**TABLE 1: Vertical Atomic Displacements  $\Delta z$  and Lateral Separation  $d$  between Pd–Pd (Zn–Zn) Rows, All Given in Angstroms and Surface Energies  $\gamma$  in  $\text{J m}^{-2a}$**

PdZn	$\Delta z(\text{Pd}^1)$	$\Delta z(\text{Zn}^1)$	$\Delta z(\text{Pd}^2)$	$\Delta z(\text{Zn}^2)$	$d$	$\gamma$ ( $\text{J m}^{-2}$ )
1 ML	0.012	−0.133	—	—	4.76	1.40
2 ML	−0.277	−0.043	0.082	−0.180	4.76	1.22
bulk	−0.127	0.077	−0.009	−0.045	4.48	1.16

<sup>a</sup> The vertical displacements of 1 and 2 ML PdZn layers are defined with respect to the positions of Pd atoms in Pd(111) layers; those of the PdZn bulk alloy are given with respect to the computed bulk-terminated geometry. The index denotes the atomic layer, starting from the surface.

density of states in the Pd 4d region for PdZn(111) and Pd(111) surfaces has been already calculated in ref 10 and resembles the experimental valence band spectra. Our calculated DOS also reproduces those of ref 10. The calculated atomically resolved local densities of states (LDOS) of Pd and Zn atoms on the PdZn bilayer surface, presented in Figure 6c, demonstrate that the STM contrast is to a large extent of electronic nature: in a relatively broad energy interval around the Fermi level the Pd electronic states clearly dominate the states of the Zn atoms.

**3.2. Thermal Desorption Kinetics of Zn Overlayers on Pd(111).** Thermal desorption spectra of Zn films deposited at 300 K, with a coverage ranging between 0.3 and 15 ML, are presented in Figure 7. The inset allows one to follow in more detail the evolution of the TD spectra for  $\Theta_{\text{Zn}} \leq 3$  ML. At Zn coverages up to 1 ML (TD spectra a–d), a single temperature desorption peak ( $\beta_2$ ) evolves, which is centered at 1040 K. With further increase of  $\Theta_{\text{Zn}}$  (TD spectra e–h), a second desorption feature ( $\beta_1$ ) appears, which exhibits a nearly coverage independent peak maximum at around 530 K, thus resembling a first-order thermal desorption. Above 3 ML (TD spectrum h), a

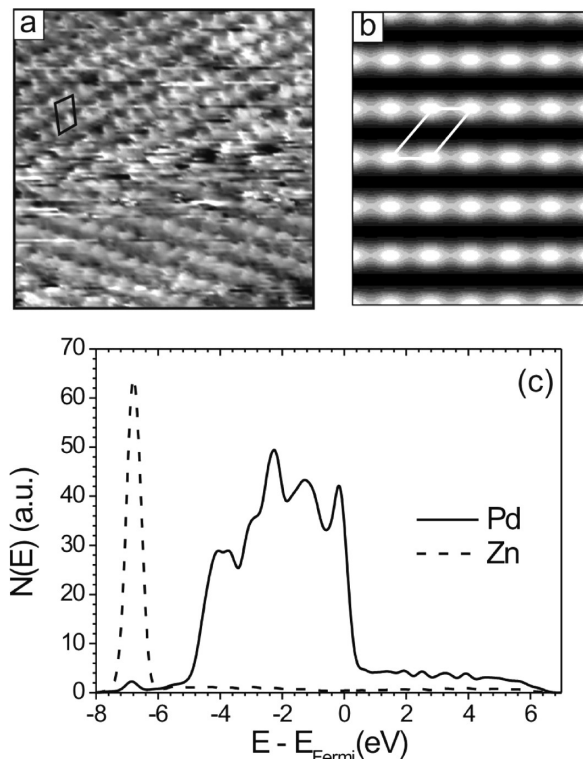


**Figure 6.** (a) High-resolution STM image of the  $(2 \times 1)$ -PdZn structure ( $50 \text{ \AA} \times 50 \text{ \AA}$ , +10 mV, 20 nA). (b) Simulated STM picture (bias voltage +0.5 V) of a 2 ML PdZn surface alloy. The  $(2 \times 1)$  unit cell is indicated on both the experimental and simulated images. (c) Calculated local density of states (LDOS) of the Pd (solid line) and Zn (dashed line) atoms on the 2 ML PdZn surface alloy.

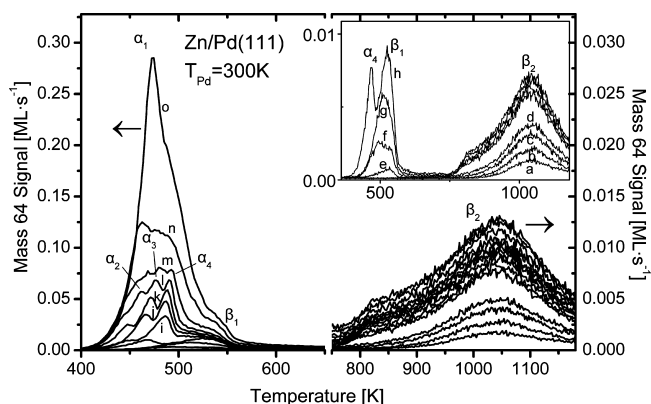


**Figure 7.** Zn TDS spectra obtained after deposition of different amounts of Zn at 300 K. The amount of Zn in ML was (a) 0.3, (b) 0.5, (c) 0.8, (d) 1.0, (e) 1.7, (f) 2.0, (g) 2.5, (h) 3.0, (i) 3.9, (j) 4.6, (k) 5.5, (l) 6.6, (m) 8.3, (n) 11.3, and (o) 15.7. The heating rate was  $2 \text{ K s}^{-1}$ .

complicated multiple peak desorption pattern is resolved between 400 and 500 K, which slightly depends on the substrate temperature during the Zn evaporation. As seen in Figure 7, there are several zero-order-like desorption states ( $\alpha_1$ – $\alpha_4$ ), which are individually characterized by common leading edges. A similar desorption of Zn has been found for thin PdZn alloy films.<sup>12</sup> An elaborate quantitative analysis of the different peaks in terms of their respective desorption energies and pre-exponential factors will be presented below. At this point it is more appropriate to correlate the thermal desorption spectra to the structural changes in the Zn overlayers after flash-annealing to selected temperatures. Figure 8 shows the evolution of STM and LEED images of 3 ML Zn films following annealing up to



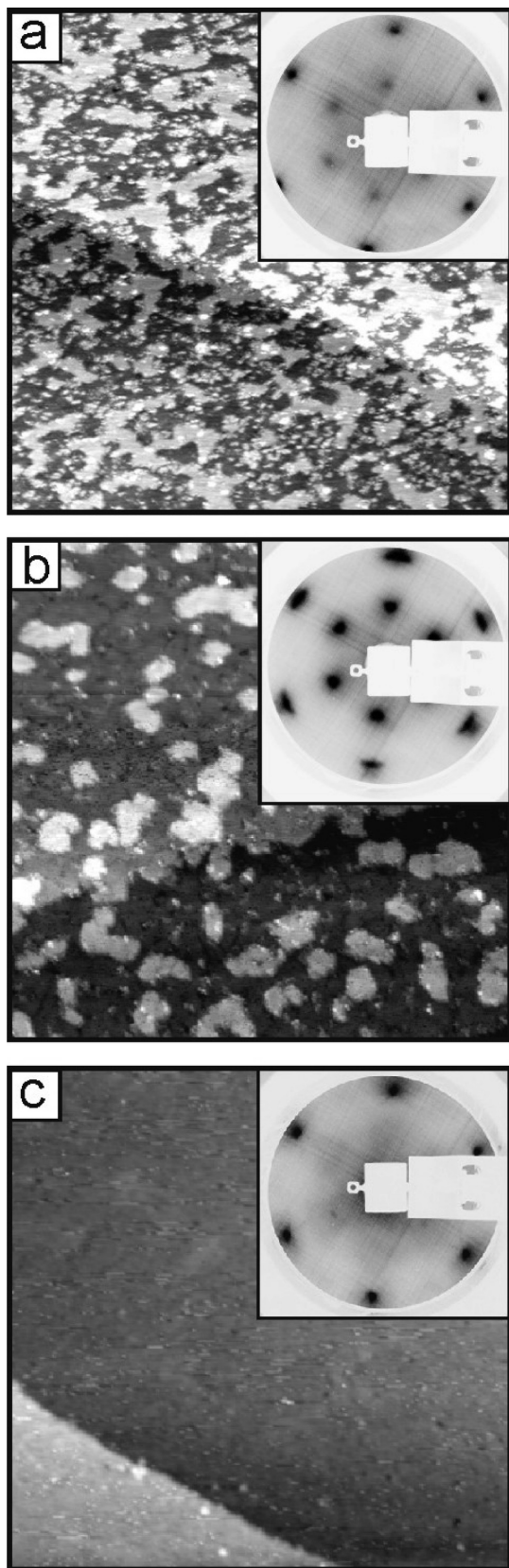


**Figure 8.** STM images of 3.1 ML Zn on Pd(111) after annealing to different temperatures: (a)  $T = 425$  K ( $1000 \text{ \AA} \times 1000 \text{ \AA}$ ,  $U = -1.0$  V;  $I = 0.4$  nA); (b)  $T = 475$  K ( $1000 \text{ \AA} \times 1000 \text{ \AA}$ ,  $U = -1.0$  V;  $I = 0.4$  nA); (c)  $T = 560$  K ( $1000 \text{ \AA} \times 1000 \text{ \AA}$ ,  $U = +1.0$  V;  $I = 0.4$  nA). The corresponding LEED patterns are shown in the insets: (a)  $E = 58.2$  eV, (b)  $E = 58.1$  eV, (c)  $E = 58.5$  eV.

560 K. Heating first to 425 K (Figure 8a), i.e., within the temperature range where the third Zn layer starts to desorb (peak

$\alpha_4$ ), causes breaking of the top Zn layer and the reappearance of the  $(2 \times 2)$  structure in the LEED pattern. Atomically resolved STM images (not shown) reveal that the islands of the top layer also exhibit a  $p(2 \times 1)$  structure, as the layers below, but with a poor structural order, in accordance with the weak and broad  $(2 \times 2)$  LEED reflexes. After heating to 475 K, which is above the desorption onset of the  $\beta_1$  peak, the STM image (Figure 8b) shows flat terraces, covered by about 30% with islands, both displaying a well-ordered  $p(2 \times 1)$  structure in high-resolution STM images (not shown), which is in agreement with the corresponding sharp  $(2 \times 2)$  LEED pattern. Note that the thermal stability of the  $(2 \times 1)$ -ZnPd alloy surface is higher for thicker (several ML) than for submonolayer Zn films. We may thus associate the  $\beta_1$  peak with the desorption of Zn atoms sitting on top of the  $(2 \times 1)$ -PdZn surface alloy layer. Further heating to 560 K results in atomically flat Pd terraces in STM images (Figure 8c) with a corresponding sharp  $(1 \times 1)$  LEED pattern. This suggests that at this temperature the Zn atoms from the  $(2 \times 1)$ -PdZn surface alloy on the Pd(111) surface dissolve into the subsurface Pd region, presumably forming dilute Pd–Zn alloy phases, before diffusing back to the Pd surface and desorbing as  $\beta_2$  peak in TDS above 800 K. Summarizing the heating behavior of 3 ML Zn films, there is a complex interplay between desorption of Zn atoms from third (peak  $\alpha_4$ ) and second (peak  $\beta_1$ ) layers and dissolution of Zn in the Pd substrate.

As mentioned above, the low temperature Zn desorption from multilayer Zn films shows several peaks  $\alpha_1$ – $\alpha_4$  which are filled subsequently with increasing Zn coverage (see Figure 7). It is remarkable that this is not simply a multilayer desorption of Zn: There are several zero-order-like desorption states ( $\alpha_1$ – $\alpha_4$ ) which are individually characterized by common leading edges, and an additional first-order-like state ( $\beta_1$ ), evidenced by a nearly coverage independent desorption peak maximum. For the analysis of these peaks, a least-squares multiple peak fit procedure was applied, which allowed the determination of the coverage and the desorption energies of the individual adsorption states. For this reason the data were fitted by summing the desorption rates obtained by simulating the Polanyi–Wigner equation<sup>35</sup> for different initial coverages, pre-exponential factors, and desorption energies for the individual desorption states. Both series of TD spectra of Zn deposited at 150 K (not shown in Figure 7) and 300 K yield within the error limits the same desorption energies. In particular, for the “true” multilayer peak ( $\alpha_1$ ), the desorption energy can be determined with a high accuracy because its leading edge is not overlapped by other peaks and the “Arrhenius” plot method for zero-order desorption is applicable.<sup>36</sup> This evaluation yields a value for the multilayer desorption energy of  $119 \pm 5 \text{ kJ mol}^{-1}$ , which is in good agreement with the literature value<sup>37</sup> for the Zn heat of evaporation of  $115 \text{ kJ mol}^{-1}$ . Since the TD spectra have been quantitatively calibrated, the intercept of the straight line in the Arrhenius plot with the Y-axis yields also the pre-exponential factor of  $1.15 \times 10^{28} \text{ atoms s}^{-1} \text{ cm}^{-2}$ . Assuming a Zn(0001) dense packed layer (surface density of  $1.62 \times 10^{15} \text{ atoms cm}^{-2}$ ), which is feasible for multilayer Zn films on Pd(111), this yields a frequency factor of  $7 \times 10^{12} \text{ s}^{-1}$ . The best fits for the desorption energies of the  $\alpha_2$ – $\beta_1$  states as obtained from Figure 7 yield  $122 \pm 5 \text{ kJ mol}^{-1}$  ( $\alpha_2$ ),  $124 \pm 5 \text{ kJ mol}^{-1}$  ( $\alpha_3$ ),  $128 \pm 5 \text{ kJ mol}^{-1}$  ( $\alpha_4$ ), and  $137 \pm 5 \text{ kJ mol}^{-1}$  ( $\beta_1$ ).

The amount of Zn bound in the individual adsorption states was evaluated for the TD series prepared at 300 K (Figure 7), which provided a rather well-defined situation. All saturation coverages of the individual adsorption states ( $\alpha_2$ – $\beta_1$ ) have been

evaluated to be  $\sim 1$  ML within an error of 20%. One has to keep in mind that the fitting procedure involving multiple parameters (coverage, pre-exponential factor, desorption energy, desorption order) is not unambiguous. However, the large number of desorption spectra measured allowed a rather reasonable data evaluation.

Another issue of interest is the desorption order of the individual states. The peak  $\alpha_1$  shows classical zero-order kinetics as characteristic for multilayer desorption. More difficult to understand is the shape of the  $\alpha_2$ ,  $\alpha_3$ , and  $\alpha_4$  peaks. All these peaks show a kinetic behavior similar to a zero-order desorption. However, the best multiple Polanyi–Wigner fits to the desorption spectra in the low temperature region of Figure 7 were obtained with a desorption order of 0.5 for  $\alpha_2$ – $\alpha_4$ . Such fractional order desorption kinetics occurs when desorption primarily takes place at the perimeter of islands or clusters.<sup>38,39</sup> The STM images from Figure 8, where 3.1 ML of Zn (where at least  $\alpha_4$  is already populated according to Figure 7) have been heated to increasing temperatures, show that islands and clusters do exist in the temperature range, where the  $\alpha_2$ – $\alpha_4$  peaks occur, supporting the fractional desorption order observed for these peaks.

As shown in Figure 7, after the removal of the multilayer states between 400 and 600 K the Zn desorption resumes above 750 K. This high temperature Zn desorption peak is centered at 1040 K and shows first-order desorption characteristics (coverage independent peak maximum). According to the Redhead approximation,<sup>35</sup> the desorption energy was calculated to be  $281 \pm 5$  kJ mol<sup>-1</sup>, assuming a pre-exponential factor of  $1 \times 10^{13}$  s<sup>-1</sup>. With increasing Zn coverage, a shoulder arises around 800 K. The large temperature gap between the high and low temperature desorption features can be attributed to the high binding energy of Zn–Pd compared to that between Zn atoms.<sup>7</sup> The Zn coverage, corresponding to the  $\beta_2$  peak, right before the  $\beta_1$  peak arises, has been estimated to be around 2 ML,<sup>16</sup> and can grow further when Zn is deposited at higher substrate temperatures ( $>700$  K) because of the Zn dissolution in the Pd bulk. This result is in contrast to the coverage of 1 ML given by Gabasch et al.,<sup>13</sup> which can be attributed to the discrepancy of the Zn coverage determination in the different studies.<sup>10,13,14</sup>

The Zn uptake, as determined by integrating the TD spectra for substrate temperatures of 150 and 300 K, is presented in Figure 9. In addition to the total Zn uptake, the development of the low temperature thermal desorption peaks ( $\alpha_1$ – $\alpha_4$  and  $\beta_1$ ) (triangles in Figure 9) and the high temperature peak ( $\beta_2$ ) (squares in Figure 7) are shown. The Zn uptake curves of the total amount (circles in Figure 9) for both sample temperatures show an identical linear increase with Zn exposure. This means that the sticking coefficient for both the 150 and 300 K sample temperature is identical and constant over the whole coverage range. Therefore, it is justified to assume that the Zn sticking coefficient is unity under these experimental conditions.

The Zn coverage is plotted further in Figure 10 as a function of the substrate temperature during the Zn deposition. In these experiments the Zn exposure was kept constant at  $\sim 4$  ML, while the substrate temperature was varied between 165 and 750 K. The total Zn coverage remains nearly constant up to 360 K and decreases beyond this temperature because of the desorption of the multilayer (see low temperature peak curve). Above 550 K the Zn uptake is mainly determined by the Pd adsorption sites: because of increased Zn diffusion into the bulk more surface Pd sites become available and therefore more Zn can be adsorbed. As a result, the total Zn coverage increases again.

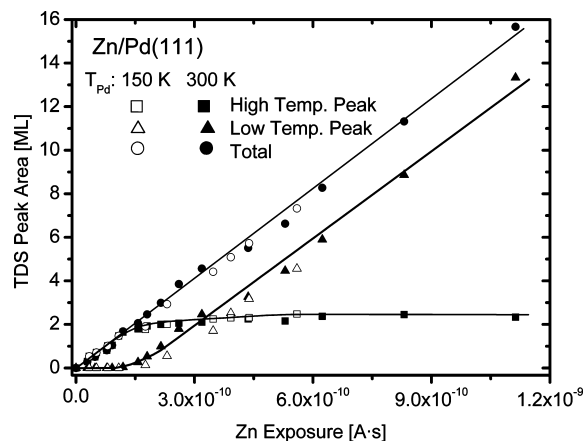


**Figure 9.** Zn coverage determined from TDS experiments versus exposure. The exposure was determined from the Zn peak in the mass spectrometer during Zn deposition. The open symbols correspond to a substrate temperature of 150 K during deposition and the full symbols to 300 K. The squares correspond to the high temperature desorption peak, the triangles to the low temperature peak, and the circles to the total coverage. The lines are just guides for the eye.

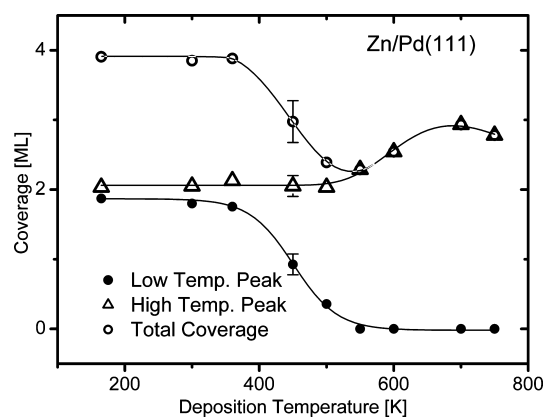


**Figure 10.** Zn coverage obtained after a Zn exposure leading to 4 ML Zn at low temperatures as a function of the substrate temperature during Zn deposition. The full circles correspond to the low temperature desorption peak, the open triangles to the high temperature desorption peak, and the open circles to the total Zn coverage. The lines are just a guide for the eye.

In the following we discuss the desorption kinetics of the high temperature peak in more detail. Since the  $\beta_2$  peak contains about 2 ML Zn, a simple first-order desorption kinetics can be excluded. Our STM data, as well as previous results,<sup>10</sup> have shown that at least two layers of a 1:1 Pd–Zn alloy form already at rather low temperatures. Therefore, one may expect that the desorption kinetics will be strongly influenced by bulk to surface diffusion of Zn and/or Pd. There are further observations which indicate that the high temperature desorption is not due to a simple first-order desorption kinetics. Ignoring the low temperature shoulder, the desorption peak  $\beta_2$  is rather symmetric relative to its maximum (see Figure 7), which is not compatible with a simple first-order desorption. Also, the full width at half-maximum (fwhm) of more than 200 K is far too broad compared to typical first-order desorption peak shapes. Lateral repulsive interactions of the adsorbed species may lead to some broadening; however, it would result in an asymmetric peak shape and cause a shift of the peak maxima toward lower temperatures with increasing coverage. Nevertheless, a change of the binding energy with the variation of the Zn coverage can be due to the fact that Zn–Pd alloys of different composition exhibit different



energetic stability, among which the 1:1 Zn–Pd alloy is energetically the most favorable one.<sup>7,8</sup>

Based on the experimental data discussed above, the following mechanism of Zn desorption can be proposed. Let us assume that at the beginning several ML of Zn are deposited onto the Pd(111) surface at low temperature (150 K). Because of the large Zn concentration gradient at the interface and the energetically favorable 1:1 ZnPd configuration, Zn already diffuses at around 300 K into the near surface Pd regions.<sup>8,10,13</sup> The Zn concentration gradient decreases throughout the progress of diffusion, and therefore the migration decelerates, especially in the deeper layers. For temperatures below 550 K, the stoichiometric PdZn layer may act as a diffusion barrier, opposing a further change in the concentration. Simultaneously, the Zn multilayers ( $\alpha_1$ – $\alpha_4$ ) begin to desorb, where the last layer ( $\beta_1$  state) corresponds to Zn atoms desorbing from the top of the Zn–Pd surface/subsurface alloy. After this, the Zn reservoir on the sample surface has been depleted and the Zn concentration gradient at the interface is now inverted. With further temperature increase ( $T > 550$  K), the decomposition of the ZnPd surface alloy starts, leading again to Zn desorption above 800 K. Because of the emerging concentration gradient, diffusion of Zn from subsurface to surface regions becomes more likely than into the bulk and continues as long as Zn exists in the surface near region. The desorption of these species can be thus related to the  $\beta_2$  peak, in particular to its high-temperature part. Our DFT calculations have shown that the energy needed to create a Zn hole in a single Zn–Pd alloy layer on the Pd(111) surface amounts to 270 kJ mol<sup>−1</sup>. Assuming a pre-exponential factor of  $1 \times 10^{13}$  s<sup>−1</sup>, a heating rate of 2 K s<sup>−1</sup>, and a first-order desorption kinetics (neglecting the actual deviation from a first order process), one can use the Redhead formula<sup>35</sup> to find that this energy corresponds to a desorption peak maximum of about 990 K, which is in good agreement with the experimental result. For the low-temperature part of the  $\beta_2$  peak we propose that it is mainly desorption rate limited. Thus the  $\beta_2$  peak desorption is influenced by both the Zn desorption rate and the Zn diffusion to the surface, leading to the deviation from a simple first-order kinetics observed from the peak shape.

Next, we want to comment on the low-temperature shoulder of the  $\beta_2$  peak around 850 K, which becomes pronounced at high Zn coverages. Here we suggest that it stems from Zn atoms which were driven into the subsurface region in excess of the 1:1 ZnPd composition already present at lower temperatures. These Zn atoms are less stable and diffuse more easily to the surface from where they desorb immediately, because the situation is now comparable to that for the  $\beta_1$  state, namely desorption of Zn atoms from the ZnPd surface alloy. A similar, but even more pronounced, peak in the same temperature region was described by Gabasch et al.<sup>13</sup> when they evaporated large amounts of Zn onto the palladium surface at 750 K, forming a bulk PdZn alloy. Additionally, they observed a significant increase of the  $\beta_2$  state with increasing Zn coverages at this substrate temperature due to alloying.<sup>13</sup>

Finally, the adsorption energies of Zn layers on top of the PdZn surface alloy have been calculated and can be compared with the adsorption energies derived experimentally. The results are listed in Table 2. Although the calculated values do not perfectly agree with the experiment, the trend of decreasing the adsorption energy for each subsequent layer of Zn on the surface alloy is well reproduced in the calculations, e.g., the large decrease in adsorption energy in going from  $\beta_1$  to  $\alpha_4$ , as well as the smaller decrease in going from  $\alpha_4$  to  $\alpha_3$  (see Table 2). The discrepancies between the experimental values and the

**TABLE 2: Adsorption Energies of Subsequent Zn Layers of Zn on the 1 ML PdZn Surface Alloy Shown in Figure 5<sup>a</sup>**

TPD peak	structure	adsorption energy, kJ mol <sup>−1</sup> calculated/experiment
$\beta_1$	1 ML Zn on PdZn (hcp and fcc)	141.8/137 ± 5
$\alpha_4$	1 ML Zn on Zn on PdZn (fcc)	112.9
	1 ML Zn on Zn on PdZn (hcp)	114.8/128 ± 5
$\alpha_3$	1 ML Zn on two Zn layers on PdZn (fcc)	109.0
	1 ML Zn on two Zn layers on PdZn (hcp)	111.9/124 ± 5

<sup>a</sup> The Zn stacking is denoted as hcp and fcc, which corresponds to ABC for pure Pd (fcc) and AB for pure Zn (hcp).

calculated values can be due to both the error from the TDS analysis and to the fact that the calculations have been done on a perfectly ordered crystal at 0 K. The Zn layer corresponding to the  $\alpha_2$  peak gave the same adsorption energy as the  $\alpha_3$  peak in the calculations. However, in this case the difference in the experimentally obtained adsorption energies is also within the error of the experiment, although the peaks can be clearly differentiated in Figure 7. The  $\alpha_1$  peak was not calculated, as this is the actual multilayer peak due to the vapor pressure of Zn. The difference in the layer stacking between fcc and hcp seen in Table 2 suggests that already the second Zn layer on the surface alloy prefers the hcp stacking of pure Zn. The observed difference in the adsorption energies of the first few Zn layers is probably due to strain effects between the different Zn layers, as the structure has to change from the distorted fcc structure of the surface alloy to the hexagonal structure of pure Zn.

#### 4. Summary and Conclusions

The growth and desorption kinetics of Zn on Pd(111) were investigated using STM, TDS, and DFT. The first atomically resolved STM images of submonolayer and monolayer films of Zn on Pd(111) showed a (2 × 1) structure in three domains, corresponding to the observed (2 × 2) LEED pattern. DFT calculations confirmed the structure and they showed that two layers of PdZn are more stable than one layer of PdZn on Pd(111), supporting the interpretation of the STM images of 0.5 ML Zn as islands with two layers of PdZn on Pd(111). After the first two layers, Zn grows in a layer by layer fashion. The TD spectra show a low temperature (480 K) Zn desorption from multilayers where the first four layers desorb with fractional order desorption kinetics with different desorption energies. DFT calculations of Zn layers on a PdZn layer on Pd(111) also showed different adsorption energies for the first Zn layers. High temperature Zn desorption (1050 K) is a mixture of diffusion limited and first-order desorption kinetics, due to desorption from Zn–Pd near surface alloys. The amount of Zn in the high temperature peak depends on the surface temperature during Zn deposition.

**Acknowledgment.** This work has been supported by the Austrian Science Funds (FWF) (P19198 and P20026) and by NAWI GASS, Graz. I.B. is indebted for support from the Hungarian OTKA 168140. H.P.K. was partly supported by a MOEL-Plus grant of the Österreichische Forschungsgemeinschaft.

#### References and Notes

- (1) Iwasa, N.; Takezawa, N. *Catal. Today* **1997**, *36*, 45.
- (2) Iwasa, N.; Takezawa, N. *Top. Catal.* **2003**, *22*, 215.

- (3) Iwasa, N.; Ogawa, N.; Masuda, S.; Takezawa, N. *Bull. Chem. Soc. Jpn.* **1998**, *71*, 1451.
- (4) Iwasa, N.; Mayanagi, T.; Masuda, S.; Takezawa, N. *React. Kinet. Catal. Lett.* **2000**, *69*, 355.
- (5) LandoltB., *Phase Equilibria, Crystallographic and Thermodynamic Data of Binary Alloys*; Springer: Berlin, 1998; Vol. 5.
- (6) Hansen, M. *Constitution of Binary Alloys*, 2nd ed.; McGraw-Hill: New York, 1958.
- (7) Chen, Z.-X.; Neyman, K. M.; Gordienko, A. B.; Rösch, N. *Phys. Rev. B* **2003**, *68*, 075417.
- (8) Chen, Z.-X.; Neyman, K. M.; Rösch, N. *Surf. Sci.* **2004**, *548*, 291.
- (9) Neyman, K. M.; Lim, K. H.; Chen, Z.-X.; Moskaleva, L. V.; Bayer, A.; Reindl, A.; Borgmann, D.; Denecke, R.; Steinrück, H. P.; Rösch, N. *Phys. Chem. Chem. Phys.* **2007**, *9*, 3470.
- (10) Bayer, A.; Flechtner, K.; Denecke, R.; Steinrück, H. P.; Neyman, K. M.; Rösch, N. *Surf. Sci.* **2006**, *600*, 78.
- (11) Fasana, A.; Abbati, I.; Braicovich, L. *Phys. Rev. B* **1982**, *26*, 4749.
- (12) Rodriguez, J. A. *J. Phys. Chem.* **1994**, *89*, 5758.
- (13) Gabasch, H.; Knop-Gericke, A.; Schögl, R.; Penner, S.; Jenewein, B.; Hayek, K.; Klötzer, B. *J. Phys. Chem. B* **2006**, *110*, 11391.
- (14) Jeroro, E.; Lebarbier, V.; Datye, A.; Wang, Y.; Vohs, J. M. *Surf. Sci.* **2007**, *601*, 5546.
- (15) Stadlmayr, W.; Penner, S.; Klötzer, B.; Memmel, N. *Surf. Sci.* **2009**, *603*, 251.
- (16) Kratzer, M.; Tamtögl, A.; Killmann, J.; Schennach, R.; Winkler, A. *Appl. Surf. Sci.* **2009**, *255*, 5755.
- (17) Tamtögl, A.; Kratzer, M.; Killmann, J.; Winkler, A. *J. Chem. Phys.* **2008**, *129*, 224706.
- (18) Kresse, G.; Furthmüller, J. *Phys. Rev. B* **1996**, *54* (11), 169.
- (19) Kresse, G.; Furthmüller, J. *Comput. Mater. Sci.* **1996**, *6*, 15.
- (20) Kresse, G.; Hafner, J. *Phys. Rev. B* **1993**, *48* (13), 115.
- (21) Kresse, G.; Hafner, J. *Phys. Rev. B* **1993**, *47*, 558.
- (22) Kresse, G.; Hafner, J. *Phys. Rev. B* **1994**, *49* (14), 251.
- (23) Perdew, J. P.; Chevary, J. A.; Vosko, S. H.; Jackson, K. A.; Pederson, M. R.; Singh, D. J.; Fiolhais, C. *Phys. Rev. B* **1992**, *46*, 6671.
- (24) Monkhorst, H. J.; Pack, J. D. *Phys. Rev. B* **1976**, *13*, 5188.
- (25) Methfessel, M.; Paxton, A. T. *Phys. Rev. B* **1989**, *40*, 3616.
- (26) Palotás, K.; Hofer, W. *J. Phys.: Condens. Matter* **2005**, *17*, 2705.
- (27) Tersoff, J.; Hamann, D. *Phys. Rev. Lett.* **1983**, *50*, 1998.
- (28) Tersoff, J.; Hamann, D. *Phys. Rev. B* **1985**, *31*, 805.
- (29) Hofer, W.; Redinger, J. *Surf. Sci.* **2000**, *447*, 51.
- (30) Hofer, W. A. *Prog. Surf. Sci.* **2003**, *71*, 147.
- (31) Perdew, J.; Burke, K.; Wang, Y. *Phys. Rev. B* **1996**, *54*, 16533.
- (32) Perdew, J.; Burke, K.; Ernzerhof, M. *Phys. Rev. Lett.* **1996**, *77*, 3865.
- (33) Dogel, J.; Freyland, W. *Phys. Chem. Chem. Phys.* **2003**, *5*, 2484.
- (34) Dogel, J.; Tsekov, R.; Freyland, W. *J. Chem. Phys.* **2005**, *122*, 094703.
- (35) Redhead, P. A. *Vacuum* **1962**, *12* (4), 203.
- (36) de Jong, A. M.; Niemantsverriet, J. M. *Surf. Sci.* **1990**, *233*, 355.
- (37) *CRC Handbook of Chemistry and Physics*, 55th ed.; CRC Press: Boca Raton, FL, 1974.
- (38) Vollmer, M.; Träger, F. *Surf. Sci.* **1987**, *187*, 445.
- (39) Chan, L.; Griffin, G. L. *Surf. Sci.* **1984**, *145*, 185.